

This work was written as part of one of the author's official duties as an Employee of the United States Government and is therefore a work of the United States Government. In accordance with 17 U.S.C. 105, no copyright protection is available for such works under U.S. Law.

Public Domain Mark 1.0

<https://creativecommons.org/publicdomain/mark/1.0/>

Access to this work was provided by the University of Maryland, Baltimore County (UMBC) ScholarWorks@UMBC digital repository on the Maryland Shared Open Access (MD-SOAR) platform.

**Please provide feedback**

Please support the ScholarWorks@UMBC repository by emailing [scholarworks-group@umbc.edu](mailto:scholarworks-group@umbc.edu) and telling us what having access to this work means to you and why it's important to you. Thank you.

# JGR Space Physics

## RESEARCH ARTICLE

10.1029/2023JA032181

### Key Points:

- The disappearing solar wind event observed at Mars in December 2022 was caused by a co-rotating interaction region
- Mars' ionosphere expanded further than previously observed locations between 2015 through 2018
- The flank ion composition boundary experiences large fluctuations in altitude after a change in the interplanetary magnetic field direction

### Supporting Information:

Supporting Information may be found in the online version of this article.

### Correspondence to:

S. R. Shaver,  
[skylar.shaver@lasp.colorado.edu](mailto:skylar.shaver@lasp.colorado.edu)

### Citation:

Shaver, S. R., Solt, L., Andersson, L., Halekas, J., Jian, L., da Silva, D. E., et al. (2024). The Martian ionospheric response to the co-rotating interaction region that caused the disappearing solar wind event at Mars. *Journal of Geophysical Research: Space Physics*, 129, e2023JA032181. <https://doi.org/10.1029/2023JA032181>

Received 15 OCT 2023

Accepted 12 FEB 2024

### Author Contributions:

**Conceptualization:** S. R. Shaver, L. Solt, L. Andersson, J. Halekas, L. Jian, R. Jolitz, D. Malaspina, C. M. Fowler, R. Ramstad, R. Lillis, S. Xu, A. R. Azari, C. Mazelle, T. Hesse

**Data curation:** S. R. Shaver, L. Solt, L. Andersson, J. Halekas, R. Lillis, S. Xu, A. Rahmati, C. O. Lee, J. P. McFadden, K. G. Hanley, D. L. Mitchell, J. R. Espley, J. R. Gruesbeck, D. Larson, S. Curry

**Formal analysis:** S. R. Shaver, L. Solt, J. Halekas, L. Jian, D. E. da Silva


















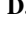






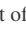
**Funding acquisition:** L. Andersson, S. Curry

**Investigation:** S. R. Shaver, L. Solt, L. Andersson, J. Halekas, L. Jian, D. E. da Silva, D. Malaspina, C. M. Fowler

© 2024. The Authors.

This is an open access article under the terms of the [Creative Commons Attribution License](#), which permits use, distribution and reproduction in any medium, provided the original work is properly cited.

## The Martian Ionospheric Response to the Co-Rotating Interaction Region That Caused the Disappearing Solar Wind Event at Mars

S. R. Shaver<sup>1</sup> , L. Solt<sup>1</sup>, L. Andersson<sup>1</sup> , J. Halekas<sup>2</sup> , L. Jian<sup>3</sup> , D. E. da Silva<sup>1,3,4</sup> , R. Jolitz<sup>5</sup> , D. Malaspina<sup>1</sup> , C. M. Fowler<sup>6</sup> , R. Ramstad<sup>1</sup> , R. Lillis<sup>5</sup> , S. Xu<sup>5</sup> , A. R. Azari<sup>5,7</sup> , C. Mazelle<sup>8</sup> , A. Rahmati<sup>5</sup> , C. O. Lee<sup>5</sup> , T. Hesse<sup>1</sup> , O. Hamil<sup>9</sup> , M. Pilinski<sup>1</sup> , D. Brain<sup>1</sup> , P. Garnier<sup>8</sup> , T. E. Cravens<sup>9</sup>, J. P. McFadden<sup>5</sup>, K. G. Hanley<sup>5</sup> , D. L. Mitchell<sup>5</sup> , J. R. Espley<sup>10</sup> , J. R. Gruesbeck<sup>10</sup> , D. Larson<sup>5</sup>, and S. Curry<sup>5,11</sup> 

<sup>1</sup>Laboratory for Atmospheric and Space Physics, University of Colorado, Boulder, CO, USA, <sup>2</sup>Department of Physics and Astronomy, University of Iowa, Iowa City, IA, USA, <sup>3</sup>Heliophysics Sciences Division, NASA Goddard Spaceflight Center, Greenbelt, MD, USA, <sup>4</sup>Goddard Planetary Heliophysics Institute, University of Maryland, Baltimore County, Baltimore, MD, USA, <sup>5</sup>Space Sciences Laboratory, University of California Berkeley, Berkeley, CA, USA, <sup>6</sup>Department of Physics and Astronomy, West Virginia University, Morgantown, WV, USA, <sup>7</sup>Now at the University of British Columbia, Vancouver, BC, Canada, <sup>8</sup>IRAP, Université de Toulouse, CNES, CNRS, UPS, Toulouse, France, <sup>9</sup>Department of Physics and Astronomy, University of Kansas, Lawrence, KS, USA, <sup>10</sup>Solar System Exploration Division, NASA Goddard Space Flight Center, Greenbelt, MD, USA, <sup>11</sup>Now at the Laboratory for Atmospheric and Space Physics, University of Colorado, Boulder, CO, USA

**Abstract** An unusually low density solar wind event was observed in December 2022 moving past both Earth and Mars. The source was traced back to a coronal hole and active region on the Sun's surface. The resulting solar wind lead to the development of a co-rotating interaction region (CIR) and trailing rarefaction region that lasted for multiple solar rotations. Within this structure, the solar wind conditions, including density, velocity, and magnetic field magnitude and orientation drastically changed. In this study we analyze the response of the Martian ionosphere using MAVEN data to these changing solar wind conditions. The low density solar wind region associated with the December event resulted in the expansion of the Martian ionospheric boundaries. We show that the ion composition boundary (ICB) is located at extreme altitudes that are beyond previously observed locations from the MAVEN mission between 2015 and 2018. Furthermore, the boundary between shocked solar wind and the Martian ionosphere identified using electron and ion data moved together on the dayside of the planet with the changing solar wind conditions. However, at the flank region these boundaries do not move together, and we show here that the decoupling of the two boundaries may be the result of a change in the interplanetary magnetic field azimuthal angle.

**Plain Language Summary** The Sun constantly emits fast moving charged particles into interplanetary space in what is known as the solar wind. In December 2022, a region of fast moving solar wind overtook a region of slower moving solar wind. The fast solar wind acted as a broom sweeping up and compressing the slower wind preceding it. This interaction of two solar wind speeds is observed to rotate with the Sun. Trailing this interaction region is a region of low density solar wind. In December 2022, this type of interplanetary solar wind structure interacted with Mars' electrically charged atmosphere, or ionosphere. Throughout this period, the ionosphere boundary characterized by a transition from solar wind ions to planetary ions moved up and down relative to the planet near dusk. As the rarefaction region passed through the system, the ionosphere expanded to unusually high heights as it was not compressed by the solar wind. However, the flapping of the ionospheric boundary seems to depend on the orientation that the solar wind interacts with Mars.

## 1. Introduction

### 1.1. The Disappearing Solar Wind Event in December 2022

The Mars Atmosphere and Volatile Evolution (MAVEN) orbiter (Jakosky et al., 2015) has been collecting valuable information on solar wind interactions with the Martian ionosphere since September 2014. MAVEN has obtained most of its measurements near solar minimum, as the maximum of solar cycle 24 had already passed at the time of MAVEN's orbit insertion. As the maximum of solar cycle 25 approaches, we are able to study the

**Methodology:** S. R. Shaver, L. Solt, L. Andersson, J. Halekas, L. Jian, D. E. da Silva

**Project administration:** S. R. Shaver, L. Andersson

**Resources:** S. R. Shaver, L. Andersson, J. Halekas, L. Jian, D. E. da Silva, R. Jolitz, D. Malaspina, R. Ramstad, R. Lillis, S. Xu, A. R. Azari, C. Mazelle, A. Rahmati, P. Garnier

**Software:** S. R. Shaver, L. Solt, L. Andersson, J. Halekas, L. Jian, D. E. da Silva, R. Jolitz, C. M. Fowler, R. Ramstad, S. Xu

**Supervision:** S. R. Shaver, L. Andersson

**Validation:** S. R. Shaver, L. Solt, L. Andersson, D. E. da Silva

**Visualization:** S. R. Shaver, L. Jian, D. E. da Silva

**Writing – original draft:** S. R. Shaver, D. E. da Silva

**Writing – review & editing:** S. R. Shaver, L. Solt, L. Andersson, J. Halekas, L. Jian, D. E. da Silva, R. Jolitz, D. Malaspina, C. M. Fowler, R. Ramstad, R. Lillis, S. Xu, A. R. Azari, C. Mazelle, A. Rahmati, C. O. Lee, T. Hesse, O. Hamil, M. Pilinski, D. Brain, P. Garnier, T. E. Cravens

effect of solar maximum conditions and activity on the Martian plasma system using MAVEN data. In December 2022, an unusual large-scale plasma structure passed through the Mars system that caused the “disappearing solar wind” (DSW) event at Mars (Halekas et al., 2023).

During the DSW event, observations from the MAVEN mission showed that solar wind proton densities dropped below 1 particles/cm<sup>3</sup> in the vicinity of Mars for roughly 24 hr. For two MAVEN orbits, the proton densities dropped below 0.1 particles/cm<sup>3</sup>. Usually, the solar wind density at Mars ranges between 1 and 10 particles/cm<sup>3</sup> (Halekas et al., 2017; Luhmann & Brace, 1991). Roughly one day prior to the DSW event at Mars, the Wind spacecraft at ~1 AU observed solar wind density, velocity, and a magnetic field configuration similar to that seen at Mars (Halekas et al., 2023). Solar wind proton densities were observed by Wind to range between 0.05 and 0.2 cm<sup>-3</sup> while the solar wind velocity stayed near ~400 km/s. For this event, MAVEN and Wind were nearly aligned radially, where Mars was 9° East of the Sun-Earth line.

Because MAVEN and Wind observed similar solar wind conditions, we infer that the DSW event was likely caused by the same large-scale plasma structure moving through the heliosphere. Stream interaction regions (SIRs) or co-rotating interaction regions (CIRs) can create conditions of compressed solar wind plasma and interplanetary magnetic field (IMF) flux tubes preceding a rarefaction region of low density solar wind (Gosling et al., 1972; Jian et al., 2006). These structures span large scales across the heliosphere and could lead to the measurements seen by both the Wind and MAVEN satellites (see Richardson (2018) and the references therein). In the days leading up to the DSW event, solar wind dynamic pressure increased and solar energetic particles (SEPs) were observed at Mars. Near Earth, Wind observed increased magnetic field strength, solar wind velocity, and densities before the period of low density solar wind. These observations can be indicative of the compression region of a CIR.

CIRs have been shown to generate events at Earth that loads and unloads plasma energy flux into the magnetosphere (Boroyev & Vasiliev, 2018; Eastwood et al., 2015; Gonzalez & Tsurutani, 1987; Tsurutani et al., 2006). The effect of these events can change the size and configuration of the magnetosphere as well as drive ionospheric currents (Baker et al., 1984). A CIR and trailing rarefaction region can lead to similar loading and unloading of energy into the Martian system (Dubinin et al., 2009; Edberg et al., 2010; Ma et al., 2014). The DSW event in December 2022 and the surrounding period of time presents a unique opportunity to study the response of the Martian ionosphere to different solar wind conditions. Analysis of this period of time can determine the important driving parameters of the Martian ionosphere.

## 1.2. The Martian Ionospheric Structure

Variations in solar wind conditions can quickly affect the Martian ionosphere because Mars' atmosphere directly interfaces with the solar wind and interplanetary magnetic field (IMF). Induced currents in the planet's ionosphere and mass loading of solar wind flux tubes causes solar wind particles to be diverted around the planet. For example, incoming IMF piles-up, stagnates, and drapes around the planet on the day-side due to their interaction with these induced ionospheric currents and through mass loading (see, e.g., Kivelson and Russell (1995); Cravens (1997); Szegő et al. (2000); Ramstad et al. (2020)). These interactions between solar wind and the planetary plasma creates an induced magnetosphere (Luhmann, 1992).

Mars is unique in that the planet also contains crustal magnetic fields that are remnant intrinsic magnetic fields from a time when the planet had a global internal dynamo (Brain, 2003; Connerney et al., 2001; Morschhauser et al., 2018). These “mini-magnetospheres” can also influence plasma dynamics inside the Martian induced magnetosphere (e.g., Brain, Halekas, et al. (2006)).

The location where Mars' ionosphere interfaces with the solar wind depends on both external drivers (e.g., solar wind conditions) as well as internal drivers (e.g., planetary ionosphere conditions, crustal magnetic fields). Instead of being a sharp transition, this interface between the planetary ionosphere and solar wind is a relatively extended region (Halekas et al., 2018; Matsunaga et al., 2017). Shocked solar wind plasma and IMF can therefore penetrate into the topside ionosphere and influence mixing dynamics in the transition region between the shocked solar wind and planetary ionosphere (Hamil et al., 2022; Mitchell et al., 2001; Xu et al., 2023).

Within this transition region exists a multitude of named boundary regions, historically based on the measurements available from specific satellites' payloads. Each of these named boundary regions indicate different

dynamical processes occurring between the Martian magnetosheath and ionosphere (Boscoboinik et al., 2020; Holmberg et al., 2019).

One of these boundary regions is the ion composition boundary (ICB), which marks the transition in the ratio between light ( $H^+$ ,  $He^{2+}$ ) versus heavy ( $O^+$ ,  $O_2^+$ ) ion species, of ions originating in the solar wind or planetary ionosphere, respectively (Breus et al., 1991; Matsunaga et al., 2017; Xu et al., 2016). The ICB has been observed near an altitude of  $\sim 650$  km at low solar zenith angles (SZA) and flares outward with increasing SZA (Holmberg et al., 2019). This boundary region also has a thickness associated with it that has been observed to range from tens to hundreds of kilometers on the dayside, and up to a few thousand kilometers in the downstream flank regions (Halekas et al., 2018). The ICB location near the flank region of the Martian ionosphere has been shown to exhibit dynamical processes and variability that can lead to discrete ionospheric plasma clouds detaching and/or being accelerated within the Martian system (Brain et al., 2010; Halekas et al., 2016, 2018, 2019).

Another named boundary region between shocked solar wind and ionospheric plasma populations is the induced magnetosphere boundary (IMB), which is also referred to as the magnetic pileup boundary (Acuña et al., 1998; Dubinin, Fränz, et al., 2006; Matsunaga et al., 2017; Vignes et al., 2000). The location where fluxes of shocked sheath electron populations (near  $\sim 50$ – $100$  eV) substantially reduce in flux defines the IMB (Lundin et al., 2004; Matsunaga et al., 2017). A rotation in the magnetic field can often be observed at this boundary as well (Bertucci et al., 2003). The IMB altitude varies between  $\sim 650$ – $800$  km at low SZA, but is often found to be almost coincident with the ICB on the day-side of the planet (Breus et al., 1991; Holmberg et al., 2019; Matsunaga et al., 2017).

The IMB and ICB represent the boundary regions of two different plasma species (electrons and ions, respectively) across the transition from shocked solar wind to planetary ionospheric plasma dominated regions. Therefore, any differences in the locations of the IMB and ICB can be used to understand dynamics across this transition region as well as the response of the Martian ionosphere to external stimuli, such as CIRs (Dubinin et al., 2009; Krishnaprasad et al., 2021).

The DSW event studied here provides an excellent opportunity to understand the effect of changing solar wind conditions on the ionospheric boundary regions. Interactions with different solar wind populations or plasma structures can create plasma instabilities and generate electromagnetic fields within the induced magnetosphere causing plasma particles to become locally accelerated (Brain et al., 2006; Dubinin, Lundin, et al., 2006; Gunell et al., 2008; Gurnett et al., 2010; Halekas et al., 2019; Lundin et al., 2011). During the event, the flank IMB and ICB are observed to move separately, which is unexpected. We analyze which solar wind conditions lead to this phenomenon.

In this study, we first identify the interplanetary structure that interacts with the Martian induced magnetosphere and ionosphere during the DSW event at Mars. We then study the effects of this structure on the Martian ionosphere. This study is structured as follows: Section 2 and 3 describe the datasets and methods used to describe the phenomena observed surrounding the DSW event. Section 4 presents a CIR and trailing rarefaction region as the solar structure that caused the DSW event in December 2022. Section 5 discusses the response of ionospheric boundary regions to the different solar wind conditions within the CIR and rarefaction region. Section 6 gives the concluding remarks on the event and the response of the Martian ionosphere to the different regions of the CIR structure.

## 2. Datasets

MAVEN at Mars is in a precessing, elliptical orbit that allows the spacecraft to sample both the solar wind and lower planetary ionosphere, depending on the orbit orientation. Mars-Solar-Orbital (MSO) coordinates are used over the period studied here to indicate the location of ionospheric boundary regions and the orientation of the IMF. MSO coordinates describe the position of the spacecraft relative to Mars and the Sun, wherein X points along the planet-sun line, with positive values indicating positions on the day-side of the terminator, Z points northward out of Mars' ecliptic plane, and Y completes the right-hand coordinate system.

Measurements from the MAVEN Solar Wind Electron Analyzer (SWEA) (Mitchell et al., 2016) were used to identify the location of the IMB along each inbound and outbound orbit segment. SWEA is a symmetric, hemispheric top-hat electrostatic analyzer designed to measure electron energy and angular distributions from 3 to



3,600 eV. SWEA covers a field of view (FOV) spanning  $360^\circ \times 120^\circ$  through the use of deflectors. The way in which these data were used to determine the IMB is described in the following section.

Observations from the Suprathermal and Thermal Ion Composition (STATIC) instrument (McFadden et al., 2015) are used to distinguish between regions of light solar wind ion species and heavier planetary ionospheric ions within the Martian induced magnetosphere and ionosphere. These measurements help identify the ICB. STATIC is a top-hat electrostatic analyzer combined with a time-of-flight velocity analyzer used to measure cold ion energies and angular distributions from 0.1 eV/q at periapsis to 30 keV/q at apoapsis and distinguish different ion species and densities at a cadence of 4 s.

MAVEN Solar Wind Ion Analyzer (SWIA) (Halekas et al., 2015) data was used in this study to indicate when the spacecraft was located in the solar wind or within the Martian magnetosheath. SWIA data was also used to show when the solar wind proton densities became unusually low during the DSW event. SWIA measures solar wind and magnetosheath ions spanning energies of 5 eV/q to 25 eV/q and fluxes of  $5 \times 10^4$  to  $7 \times 10^{11}$  eV/(cm<sup>2</sup> s sr eV). Coarse data, used in this study, covers a  $360^\circ \times 90^\circ$  field of view with a  $22.5^\circ$  resolution (Halekas et al., 2015).

Measurements from the MAVEN Solar Energetic Particle (MAVEN/SEP) instrument (Larson et al., 2015) are used to indicate the CIR compression region in the vicinity of Mars. MAVEN/SEP onboard MAVEN consists of two solid-state detector telescopes that measure electrons from 20 keV/q to 200 keV/q and ions from 20 keV/q to 6 MeV/q within a  $42^\circ \times 31^\circ$  field of view. MAVEN/SEP observations can be used to indicate solar activity and to discern solar influence and energy input into the Martian magnetosphere and atmosphere (Lee et al., 2017, 2018). MAVEN/SEP electron and ion fluxes are measured at a cadence between 1 and 8 s depending on data rates. In analysis of the SEPs surrounding the DSW event, level 1 energy fluxes from the forward and reverse look directions of the telescope were integrated over all MAVEN/SEP energies. These integrated fluxes of both detectors 1 and 2 were then averaged to gather the total energy flux of charged particles accelerated by the CIR at a particular time. We only included MAVEN/SEP measurements with the attenuator in the open state to remove instrument artifacts in the measurements. The energy flux results were then smoothed over 1 min to better show the increase of SEPs surrounding the DSW event.

Data from the Magnetometer (MAG) instrument (Connerney et al., 2015) onboard MAVEN was used to compute magnetic pressure, identify crossings of ionospheric boundaries, as well as determine the IMF configuration over the period of time studied. The MAVEN MAG instrument is a dual set of tri-axial fluxgate magnetometers. MAG determines the ambient vector magnetic field over a range of  $\pm 65,536$  nT with a resolution of up to 0.008 nT. MAG samples the ambient magnetic field in three dimensions at a cadence of 32 samples/second. The 1 s resolution data was used for analysis in this study.

The Wind satellite has been positioned at the Earth-Sun L1 Lagrangian point since May 2004, and observed this event near 1 AU roughly 1 day before the event passed by Mars (Halekas et al., 2023). Wind's ion electrostatic analyzers (PESA) (Lin et al., 1995) provide 3D measurements of interplanetary proton populations for energy ranges from 3 to 30 keV/q. These measurements are used in this study to show instances of the unusually low solar wind density events from December 2022 through June 2023. Ion data from Wind's Solar Wind Experiment (SWE) (Ogilvie et al., 1995) was used to estimate the velocity and density of the solar wind during this period of time.

Magnetic field data from the Wind Magnetic Field Investigation (MFI) instrument was used to detect the start and end of the CIR (Lepping et al., 1995). An RTN coordinate frame used to describe the magnetic field vector components. In this frame, the R direction points radially outward from the Sun, T lies along the orbital direction of the Wind spacecraft at roughly 1 AU, and N points northward such that the RN plane lies along the solar rotation axis.

The Air Force Data Assimilative Photospheric flux Transport and Wangley-Sheeley-Arge (ADAPT-WSA) ensemble set of solutions was utilized to trace footpoints of the emanating location of the incident solar wind at Mars back to the solar surface (da Silva et al., 2023).

### 3. Methods

#### 3.1. ICB Location Determination and Statistical Analysis

The changes in the ICB location are used to analyze ion dynamics during the times surrounding the DSW event at Mars. The ICB is determined using STATIC (McFadden et al., 2015) c6 level 2 differential energy and mass flux

data product. The ratio of  $O^+$  and  $O_2^+$  to  $H^+$  and  $He^{2+}$  fluxes was used to determine the location of the ICB. Where this ratio equals one marks the transition across the ICB. Because STATIC counts for a particular AMU are determined using a Gaussian function, a range of mass bins are employed to define fluxes for  $H^+$ ,  $He^{2+}$ ,  $O^+$ , and  $O_2^+$ . The ranges used for this study are given in Table S1 in Supporting Information S1.

Due to the potential motion of the plasma across the boundary, temperature differences across the different ion species, the speed and angle of the spacecraft as it traverses across this boundary, the thickness of the ICB, the cadence to get ion measurements, limitations in the instrument field of view, and so forth, this transition from light to heavy ion species is not always sharp. Therefore, a region containing the ICB was identified manually on each inbound and outbound orbit segment. Within this region, the mass energy flux ratio between light and heavy ions must transition across a value of one. At higher altitudes relative to the manually identified ICB region, there must be increased ion fluxes with energies greater than 100 eV to indicate the sheath region. At lower altitudes relative to the transition period, there must be increased ion fluxes with energies near or below 10 eV. This ensures that the spacecraft has moved from a higher energy sheath population of ions into the cold ionospheric ions. At the same time, the mass energy fluxes indicate a transition from low masses in the sheath region to higher mass ions in the planetary ionosphere.

An automated routine was then applied within this manually identified ICB region, which determines the heavy-to-light ratio from STATIC ion counts rather than energy flux. Counts are used to decrease any bias in the composition ratio that may be due to high energy ions. Within the manually identified transition period, we determined each time the mass count ratio crossed a value of one. If more than one crossing was identified, the median time of these unity crossings within the transition period was used to mark the ICB. We determined the statistical error in the ratio by adding the statistical error of the fluxes of the component ion species in quadrature. This ratio error did not exceed 100% and was often below 50%. In order to account for manual identification errors, we set the location error bounds to be where the heavy-to-light ratio is 0.2 (lower altitude bound) and 5.0 (upper altitude bound). This error, indicating a 500% change in the mass ratio, was large compared to other errors looked at. Examples of the detected ICBs and associated errors are included in Supporting Information S1.

In this study, we used this identification technique for the ICB for two means of analysis. First, we conducted a statistical study spanning over 7500 ICB locations identified on inbound and outbound orbit segments between January 2015 and December 2018. The second analysis identified the ICB location in December 2022 to evaluate the effects of the DSW solar structure on this transition region.

### 3.2. IMB Location Determination

The IMB was determined in order to compare the aforementioned ICB (i.e., the boundary between ion populations) with the boundary between shocked solar wind and ionospheric electron populations. The IMB has historically been defined in different ways across different studies. In this work, we attempt to combine these techniques to identify the IMB to obtain a complete time history of both the IMB and ICB locations surrounding the DSW event. The IMB was therefore identified manually from 22 December 2022, through 31 December 2022, using primarily the SWEA electron energy flux spectrograms alongside the MAG, and SWIA energy flux measurements along each inbound and outbound orbit segment. The IMB was manually identified as follows: a local minimum in the SWEA electron fluxes in the 30.9–78.4 eV energy ranges was first determined. Simultaneously, SWIA proton fluxes needed to decrease in mean energy and total flux (following Ramstad et al. (2017)). Magnetic field fluctuations had to increase on average moving toward higher altitudes, and magnetic field strength had to increase moving toward lower altitudes (following Bertucci et al. (2003)). The magnetic field fluctuations were characterized along each orbit by taking the standard deviation of the magnetic field strength over 8 s. At or just below the inbound IMB, a spike in the standard deviation of  $|B|$  corresponding to a rotation in the magnetic field was sometimes observed. This may be associated with the current sheet often found at the IMB (Bertucci et al., 2005). Occurrences of such a spike were ignored to determine if fluctuations increased moving toward higher altitudes. Finally, across this determined boundary the characteristic peak sheath energy in the SWEA electron distribution function had to move below 20 eV.

We also used a semi-automated routine to strengthen the positioning of the IMB. We first smoothed the SWEA energy fluxes in each of the 30.9–78.4 eV energy ranges over 20 s increments. From an arbitrary location in the sheath region, we then found where the smoothed energy fluxes in each of the studied bins decreased by a factor of

1.8 relative to those in the sheath. The lowest altitude where this condition was met was used as the IMB location. This follows the routine used by Lentz et al. (2021).

During the DSW event, this factor of attenuation was decreased to 1.5 and the energy bins from 43.6 to 98.9 eV were used to determine the attenuation. Orbits 17,882 (1.5), 17,883 (1.5), 17,883 (1.5), 17,892 (1.5), 17,897 (1.6), 17,900 (1.3), and 17,902 (1.1) also had to use a decreased attenuation factor indicated in the parenthesis. We ensured that the SWEA electron distribution function characteristic peak sheath energy was no longer observed across these identified boundaries.

Both identification methods (manual and semi-automatic) were employed three times to determine the IMB. The average of these six locations was used as the IMB location, and the standard deviation of the determined boundary locations was used as the error on the IMB. Examples of the IMB determination are shown in Supporting Information S1.

## 4. The DSW Corotating Interaction Region

### 4.1. Evidence of a CIR at Wind/Earth and Its Solar Source

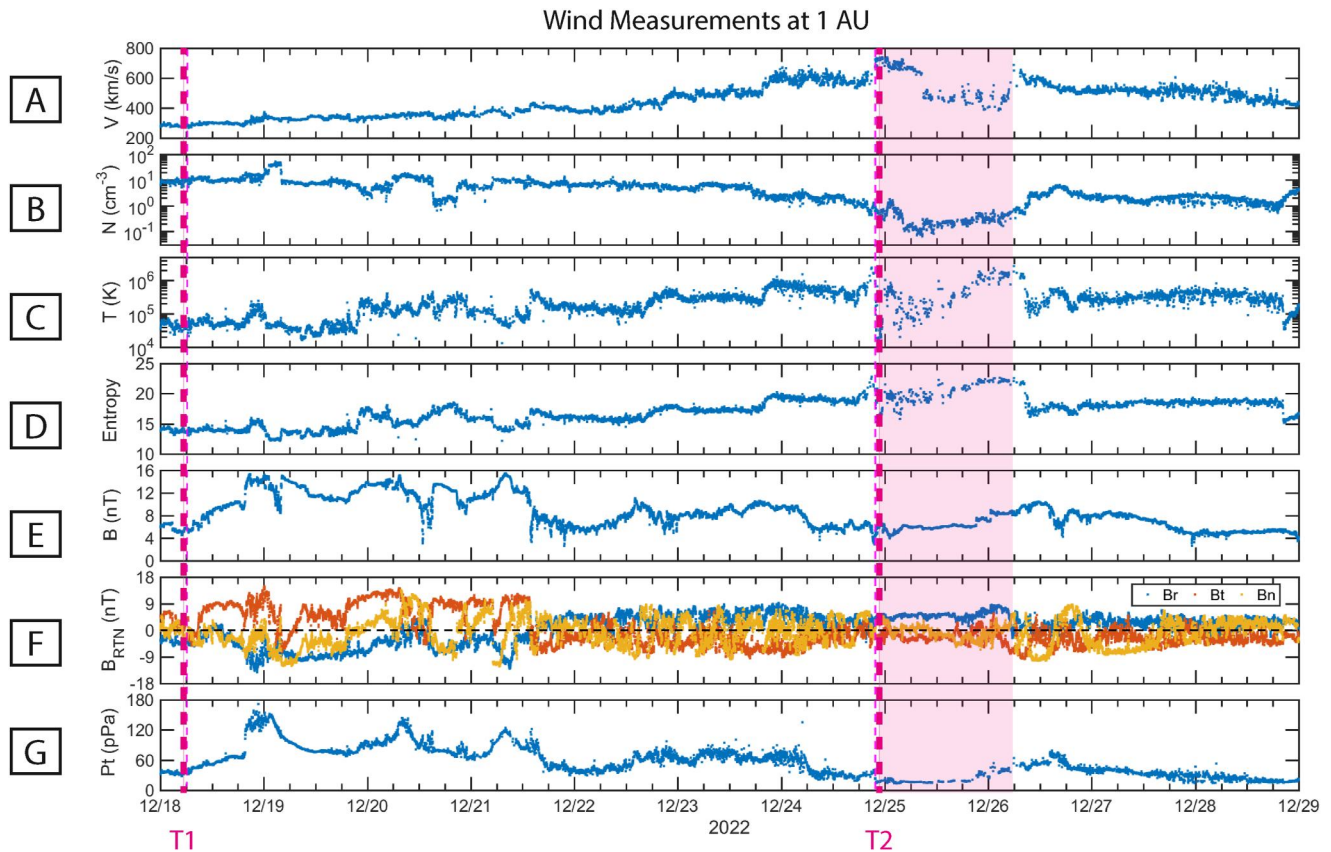
During the DSW event at Mars, pristine solar wind conditions were not directly sampled by MAVEN (Halekas et al., 2023). Therefore, observations from the Wind satellite are used to determine the structure that caused the event because Earth and Mars were nearly aligned radially during this time. Figure 1 depicts solar wind plasma measurements made by Wind at 1 AU from December 18–29, 2023. The period of low solar wind proton density (Panel b) occurs on December 25 at 1 AU, which is indicated by the shaded pink region in Figure 1.

Leading up to this period of low solar wind proton densities, solar wind measurements indicate the presence of a stream interaction region (SIR). Indicators of a SIR structure in the 1 AU Wind data shown in Figure 1 include: an increase in solar wind velocity  $V$  (panel a), an increase and then decrease of proton number density  $N_p$  (panel b), an increase in proton temperatures (panel c), the increase of specific proton entropy calculated as  $\ln(T_p^{3/2}/N_p)$  (panel d) (Neugebauer et al., 2004), a compression of the magnetic field  $B$  (panels e, f), and the pile-up of total pressure,  $P_t$ , which is the sum of magnetic and thermal plasma pressure (panel g) (Jian et al., 2006, 2011, 2019). The magnetic pressure is calculated as  $B^2/2\mu_0$  and the thermal pressure as  $nk_B(T_p + Te)$ , assuming quasineutral conditions. The approximate start and stop times of the SIR (T1, T2) are marked on Figure 1 by vertical dashed pink lines. No near-Earth interplanetary coronal mass ejections were listed during this period in the Cane and Richardson (2003) catalog, supporting the notion that a SIR likely caused this event (Richardson & Cane, 2010).

SIR structures arise as a compression region in solar wind plasma as fast solar wind overtakes the preceding slower solar wind (Owens, 2020; Parker, 1965; Sarabhai, 1963). This creates a pile-up of solar wind plasma and IMF within the SIR, which is then usually followed by a rarefaction region of low-density solar wind plasma. The rarefaction region following a SIR could be the cause of the low proton densities observed during the DSW event at Mars. The compression region of the SIR depicted in Figure 1 is shown to last for nearly 8 days from December 18–24, which is an unusually long period (Huang et al., 2019; Jian et al., 2006). This period is designated as the SIR due to the observed properties mentioned in the previous paragraph; however, it is noted that other transient features may be responsible for parts of the observations within T1 and T2. Such features may have implications for the unusually low-density solar wind within the trailing rarefaction region, but analysis is outside the scope of this study.

Panel (a) of Figure 2 shows a schematic of a general SIR structure based on a diagram from Hundhausen (1972). Here, the Sun rotates counterclockwise, and the blue and pink lines represent the IMF lines carrying slow and fast-moving solar wind, respectively. The stream interface indicated by the solid black line separates the solar wind of differing speeds. The SIR compression region is indicated by the light blue-filled region surrounding the stream interface. The pink dotted lines trailing the fast wind depict the rarefaction region of low-density solar wind that usually follows the SIR.

If interactions (e.g., collisions, instabilities) between particles within the solar wind do not occur fast enough to dissipate the compression region between slow and fast-moving solar wind before a solar rotation is completed, then the structure can become a CIR (Richardson, 2018; Smith & Wolfe, 1976). CIRs are SIRs that are observed at the cadence of around one solar rotation (Snyder et al., 1963).



**Figure 1.** Solar wind plasma measurements from the Wind satellite in orbit near 1 AU. Panel (a) depicts solar wind proton velocity. Panel (b) depicts solar wind proton densities calculated using the nonlinear fitting of the SWE instrument measurements. Panel (c) represents the solar wind proton temperatures. Panel (d) shows the specific entropy. Panel (e) depicts the magnitude of the magnetic field in [nT]. Panel (f) shows the direction of the magnetic field in RTN coordinate frame. Panel (g) depicts the total pressure (magnetic and thermal) calculated using these measurements. The period between T1 and T2 marked with vertical pink dashed lines indicates the CIR compression region. The shaded pink region depicts the trailing rarefaction region with low solar wind densities.

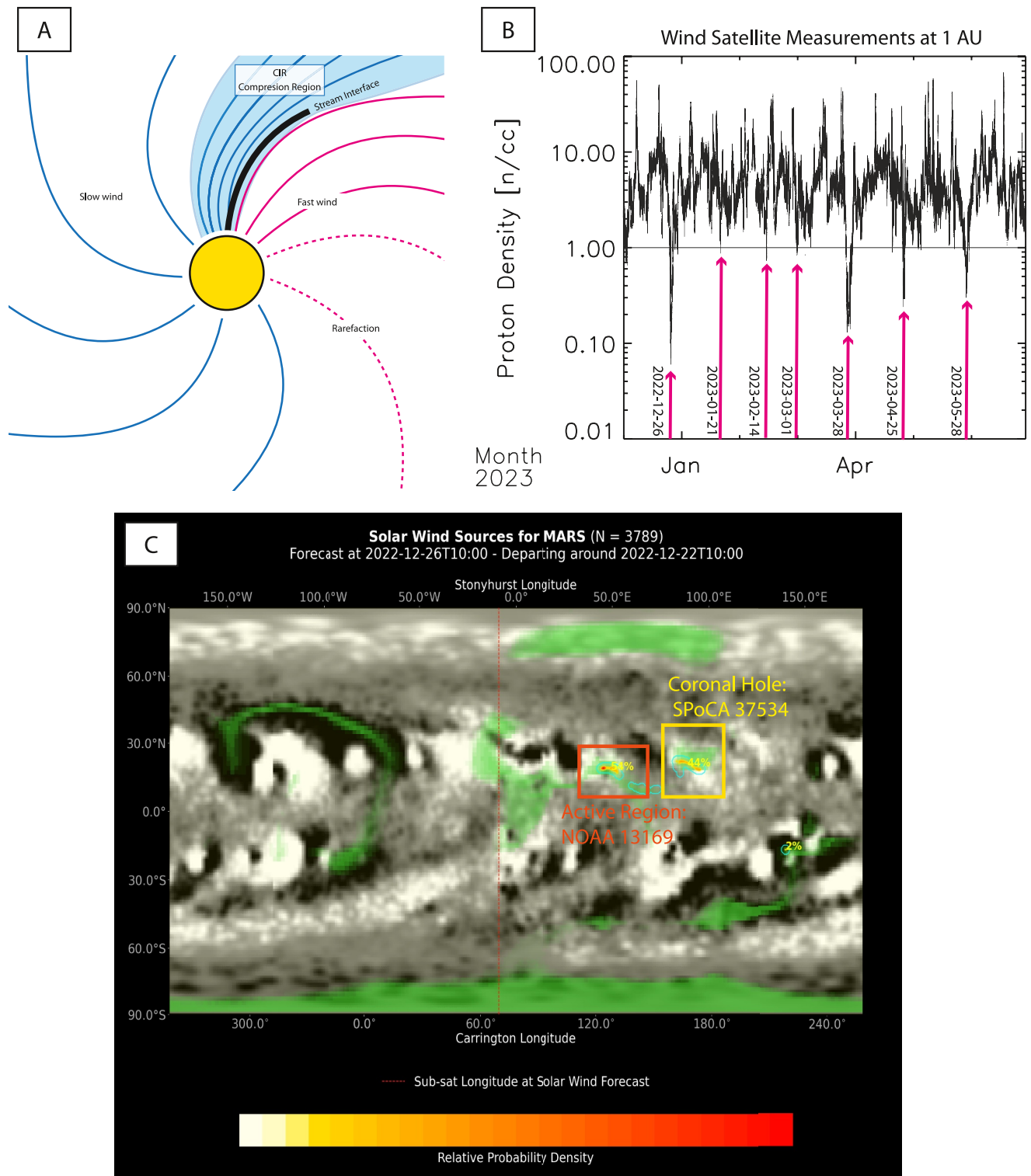
The cadence of the low-density solar wind events in Figure 2b provides evidence that the SIR structure that caused the DSW event at Mars is, in fact, a CIR. This figure depicts the time history of solar wind proton densities from the Wind satellite at 1 AU spanning December 2022 through June 2023. The black horizontal line on this plot indicates a density of 1 particle/cm<sup>3</sup>. Each pink arrow indicates a time when the solar wind proton densities dropped below 1 particle/cm<sup>3</sup>. If the densities dropped below 1 particle/cm<sup>3</sup> multiple times within 7 days of one another, only the minimum of those density drops were pointed out for this figure.

Starting with the December 26th DSW event, subsequent events occurred at a cadence of 25, 23, 15, 26, 28, and 33 days after one another. The deepest events observed in December 2022 March 2023, April 2023, and May 2023, show similarities in the density and velocity structures. Therefore, the solar structure with unusually low proton densities at 1 AU in December 2022 is likely due to the rarefaction region of a CIR.

The unusually low proton density of the rarefaction region during the DSW event may be a consequence of the solar footpoints that the CIR emanates from. Solar wind can emanate from coronal holes and from active regions (Kojima et al., 1999; Luhmann et al., 2002; Stansby et al., 2021). Panel (c) of Figure 2 depicts a snapshot of the distribution of source locations at the Sun (1 solar radii) that connect to Mars during the DSW event on December 26 using an ensemble set of solutions obtained from ADAPT-WSA (da Silva et al., 2023). The varied dimensions of the ensemble set include ADAPT photospheric maps, perturbations in forward-mapping departure location, and a time window of  $\pm 12$  hr for included arrivals of propagated parcels to Mars.

This distribution indicates that the source of the solar wind for this event emanated from the Sun on 22 December 2022, and has two possible surface locations from which it originated. About half of the solar wind source could





**Figure 2.** Figure depicting evidence for the corotating interaction region (CIR) structure that caused the DSW event at Mars and at Earth. Panel (a) shows a schematic of a CIR, or CIR, as a compression region between slow and fast-moving solar wind (Hundhausen, 1972; Owens, 2020). Panel (b) depicts solar wind proton densities from December 2022 through June 2023 using the Wind satellite. Dates where the solar wind proton density drops below 1 particle/ $cm^{-3}$  are indicated with a pink arrow. Panel (c) shows the ADAPT-WSA ensemble set of solutions (da Silva et al., 2023) depicted the solar footpoints where the solar wind is predicted to have emanated from on 26 December 2022, at Mars.

have originated from a coronal hole (SPoCA 37534), indicated by the yellow box. The other half could have originated from an active region (NOAA 13169), indicated by the red box. Previous solar wind disappearance events have traced the solar wind footprints back to locations where a coronal hole is found next to an active region on the solar surface, just as we observe in this DSW event (Janardhan, Fujiki, et al., 2008; Janardhan, Tripathi, & Mason, 2008).

The coronal hole and active region source locations can influence the composition and structure of the resulting solar wind (Bale et al., 2023; Hudson et al., 2022). This in turn can affect the dynamics of the Martian induced magnetosphere. Coronal holes are regions of open magnetic field lines on the Sun (Cranmer, 2009; Zirker, 1977), and active regions are where the Sun's magnetic field is perturbed (Van Driel-Gesztelyi & Green, 2015). Active regions can produce large solar events, such as flares and coronal mass ejections, and are often associated with dynamic magnetic field activity.

Solar wind charge-state ratios can help determine the solar wind source location (Bürge & Geiss, 1986). The low  $O^{7+}/O^{6+}$  charge-state ratio determined from the Solar Wind Ion Composition Spectrometer (SWICS) 2.0 level 2 data (SWICS 2.0 Level 2 Data Documentation, 2007) on the Advanced Composition Explorer (ACE) (Stone et al., 1998) indicates a coronal hole source of the solar wind near 1 AU on December 22–25 (Zurbuchen et al., 2002). However, the charge state ratios of  $O^{7+}/O^{6+}$ ,  $C^{6+}/C^{5+}$ , and the average Iron charge state ( $Q_{Fe}$ ) increase as the DSW event passes by Earth on December 25 and 26. While these ratios are higher than nominal coronal hole values during the DSW, they are not high enough to definitively indicate an interplanetary coronal mass ejection as the source (Heidrich-Meisner et al., 2016; Lepri et al., 2001; Richardson & Cane, 2004). A detailed follow-up study is being conducted on this issue, so we end our discussion here.

The heightened ratios may indicate that the solar wind during the unusual DSW emanated from an active region. This event occurred as solar cycle 25 approaches maximum when roughly 40%–60% of the solar wind has been shown to come from active regions (Schrijver & DeRosa, 2003; Stansby et al., 2021). This may have implications for the IMF configuration that interacts with the Martian system over this period.

#### 4.2. Evidence of the CIR and Rarefaction Region at Mars

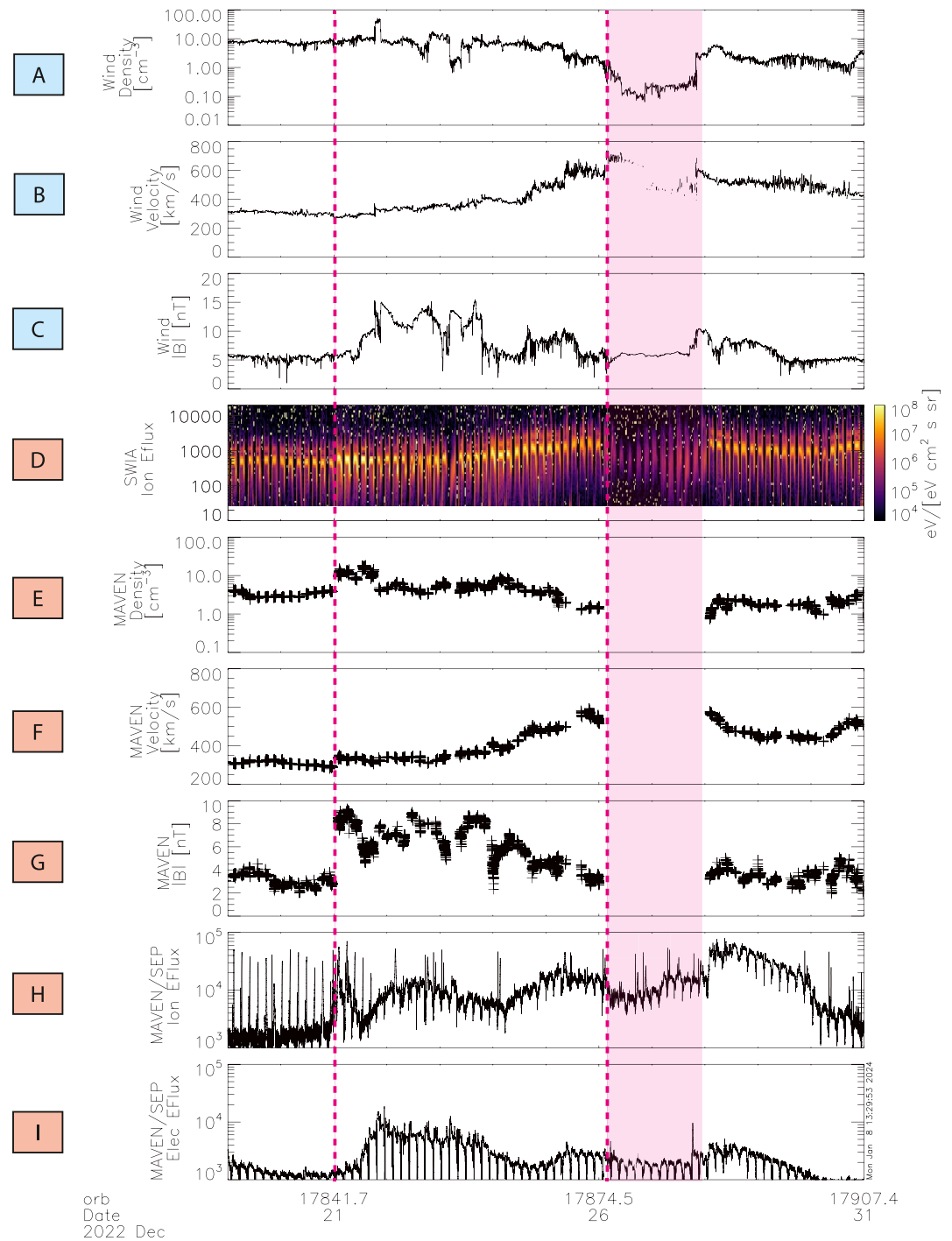
The juxtaposition of the CIR compression region preceding the extremely low density solar wind rarefaction region can be used to study the effects of opposing solar wind driving conditions on the Martian induced magnetosphere over a few days. MAVEN data compared with data from Wind in the surrounding dates can be used to determine when and how the CIR and rarefaction region influenced the Martian system.

Figure 3 depicts Wind measurements that have been shifted ballistically from 1 AU to Mars (panels a–c) (see Halekas et al. (2023) and references therein for more details on the method) along with MAVEN plasma measurements (panels d–j). Panel letters within a blue box refer to the Wind measurements, and those within a red box refer to MAVEN measurements. Panels a, b, and c show the solar wind proton density, velocity, and magnetic field magnitude measured by the Wind satellite at 1 AU that have been shifted forward in time by one day and out to Mars' orbit. Panel d depicts solar wind ion energy fluxes from the MAVEN SWIA instrument, where brighter colors indicate higher fluxes. Panels e, f, and g depict the solar wind density, velocity, and magnetic field magnitude computed using the upstream solar wind database described in Halekas et al. (2017). Panel h shows MAVEN/SEP ion energy fluxes averaged from detectors 1 and 2, respectively. Panel i depicts MAVEN/SEP electron energy fluxes averaged over detectors 1 and 2. The spikes in MAVEN/SEP ion energy fluxes (panel h), especially prevalent before T1, are due to "Mars shine," or reflected sunlight from the disc of Mars, which induces electronic noise in the instrument when the FOV includes the illuminated surface of Mars. The proposed CIR start (T1) and stop (T2) times are indicated by the vertical pink dashed lines in Figure 3. The rarefaction region with lower-than-usual solar wind proton densities at Mars lasted for nearly 2 days from December 26–28, and is indicated in Figure 3 by a pink-tinted period of time.

Evidence of the CIR compression region interacting with the Martian system before the DSW event can be seen in the increase and then decrease of the solar wind ion number density (panel e) between T1 and T2, as well as the increase in solar wind velocity (panel f) and IMF magnitude (panel g). These MAVEN measurements show similar solar wind features as those observed with the Wind spacecraft (panels a, b, and c).

Furthermore, heightened fluxes of SEPs have been shown to exist in the compression region of a CIR (Richardson, 2004; Thampi et al., 2019). Before the DSW event, MAVEN/SEP electron fluxes (Panels i, j)





**Figure 3.** This figure depicts plasma measurements made by Wind (blue indicator) and MAVEN (red indicator) from 19 December 2022 through 31 December 2022. These measurements provide evidence of the CIR and rarefaction region interacting with the Martian system. The CIR interacts with Mars between times T1 and T2, as indicated by the vertical dashed pink lines. The rarefaction region following the CIR is indicated by the shaded pink region. The repeating temporal signatures in the MAVEN data at periods of ~3–4 hr are due to the MAVEN orbit moving inside and outside the Martian induced magnetosphere.

increased over December 21–24. An increase in MAVEN/SEP electrons was observed between the proposed CIR start and stop times (T1 and T2). MAVEN/SEP ion fluxes (panel h) also increased over this period near the leading edge of the CIR (at T1) through the rarefaction region.

The DSW event at Mars occurs within the rarefaction region that trails the CIR. The end of the CIR and start of the rarefaction region occurs at T2, which is indicated by the maximum in solar wind velocity measured with the Wind satellite (panel b). Solar wind ion fluxes measured using the MAVEN SWIA instrument (panel d) decrease in the rarefaction region.

The low solar wind densities can affect the dynamics of the Martian induced magnetosphere and ionosphere. For example, within the rarefaction region at Mars, a dropout in solar wind density and velocity computed using MAVEN upstream solar wind moments from Halekas et al. (2017) is observed (Panels e and f of Figure 3), leading to a decrease in solar wind dynamic pressure. The lack of compressing solar wind dynamic pressure can permit the expansion of the Martian induced magnetosphere.

The different solar wind conditions within the compression region of the CIR and following unusually low density rarefaction region offers an excellent opportunity to study the effect of contrasting solar wind conditions on the dynamics within the Martian induced magnetosphere. As shown in Figure 3, this period of time allows analysis of the Martian system's response to a change from high to low dynamic pressure driven by changes in solar wind density and velocity.

## 5. The Response of the Martian Ionosphere

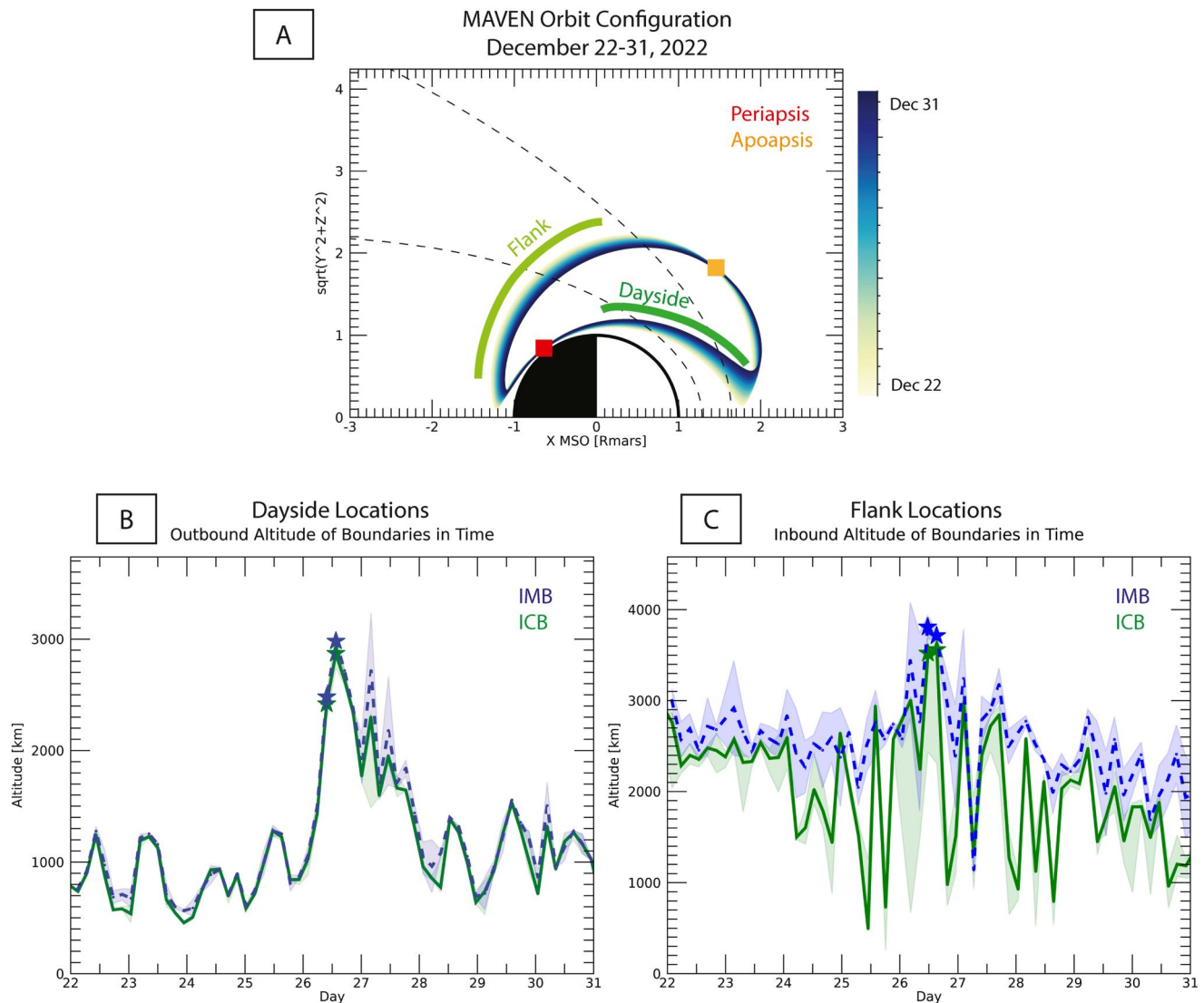
The orbit configuration of MAVEN from December 22–31, 2022, allowed for a detailed study of the ionospheric boundary regions near both the subsolar and flank region of the Martian induced magnetosphere. Figure 4 panel a depicts MAVEN's orbit in MSO over this period and indicates that the MAVEN orbit did not process much when the CIR and rarefaction region passed by Mars. MAVEN's periapsis was observed near a SZA of  $\sim 132.8^\circ$  and an areographic latitude of roughly  $-42^\circ$  (near the strong crustal magnetic fields). From December 22–31, the outbound portion of the MAVEN orbit covered mostly day-side ( $X_{\text{MSO}} > 0$ ) locations, whereas the inbound portion of the orbit occurred mainly on the night-side ( $X_{\text{MSO}} < 0$ ) of the planet (see Figure 4 panel a).

Therefore, to study the response of the Martian ionosphere on the dayside ( $\text{SZA} < 80^\circ$ ) and flank regions ( $\text{SZA} \geq 80^\circ$ ) to the CIR compression and rarefaction regions, analysis of the IMB and ICB has been broken up into outbound and inbound orbit segments. Panels b and c of Figure 4 depict the time history of IMB (blue) and ICB (green) altitudes from December 22–31. Panel b shows the IMB and ICB altitudes along the outbound portion of each MAVEN orbit, and panel c depicts the boundary regions' altitudes along the inbound portion of the orbit. Each observation point is connected by a straight line to show the direction of change in boundary altitude from one orbit to the next.

At low SZAs (Figure 4, panel b), the ICB and IMB boundary regions clearly vary in altitude similarly from orbit to orbit, expanding and contracting together. The IMB is located at slightly higher altitudes than the observed ICB from December 22–31; however, the two boundary regions observed along the outbound orbit rise and fall at roughly the same rate. During the DSW event on December 26, the two boundary regions at low SZA expand to high altitudes. The IMB is located at a maximum altitude of  $\sim 2,900$  km at  $\sim 12^\circ$  SZA, and the ICB at a maximum altitude of  $\sim 2,900$  km at  $10^\circ$  SZA. The altitudes of the IMB and ICB during the two DSW event orbits are marked using blue and green stars, respectively, in Figure 4. These altitudes extend past the nominal bow shock location derived from Vignes et al. (2000) at low SZAs.

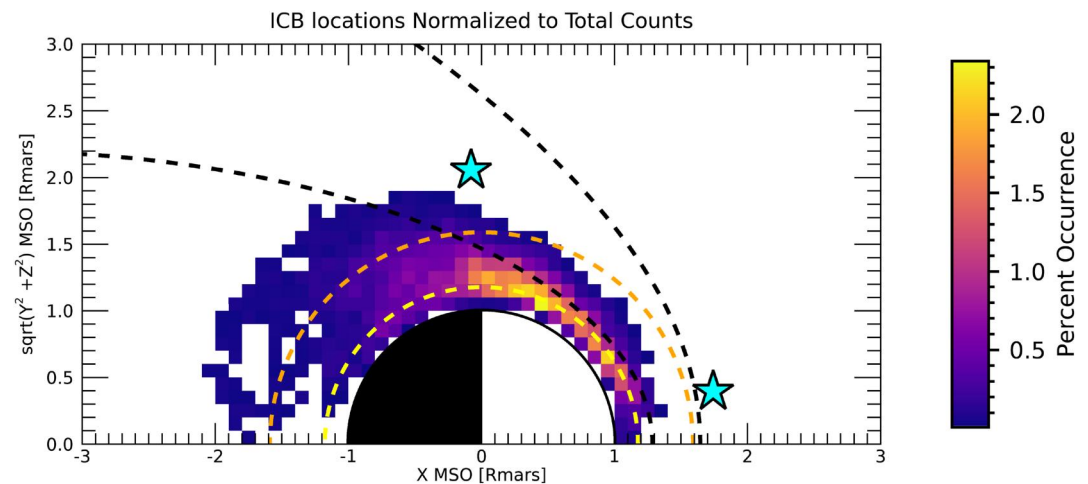
The IMB and ICB observed at the flanks, however, seemingly exhibit a decoupling in their locations relative to one another (see Figure 4, Panel c). From 12/22 to 12/24 the two boundary regions expand and compress roughly 500 km in altitude on timescales of 1–2 MAVEN orbits ( $\sim 3.5$ –7 hr). Although the IMB is found at higher altitudes than the ICB over these 2 days, the two boundary regions exhibit similar oscillatory altitude changes. Then on December 24, the IMB and ICB are initially both compressed before appearing to decouple significantly for most of the day, separating by almost 1,000 km. The flank ICB altitude continues to fluctuate over 500–1,500 km between orbits, while the flank IMB does not experience these large fluctuations in altitude (Figure 4, Panel c).

Within the rarefaction region trailing the CIR from December 26–28, the flank IMB and ICB continue to exhibit different altitude signatures in time. Only during the two minimum DSW proton orbits on December 26 do the flank IMB and ICB expand together and remain relatively fixed at a high altitude. The IMB expands to a maximum altitude of  $\sim 3,800$  km at  $\sim 87^\circ$  SZA, and the ICB to  $\sim 3,600$  km at roughly  $92^\circ$  SZA. This is shown by the starred points in Figure 4.



**Figure 4.** Observed altitudes of the ICB shown in green and IMB shown in blue in the period surrounding the DSW event. Panel a depicts the precession of the MAVEN orbit from December 22 to 31, 2023. Lighter colors indicate orbits occurring earlier in time, whereas darker colors indicate orbits occurring later in time. Periapsis is indicated by a red square, and apoapsis by an orange square. The outer and inner black dashed lines are used to indicate the modeled locations of the bow shock and magnetic pileup boundaries, respectively, from Vignes et al. (2000). As shown in this figure, MAVEN's orbit did not precess much over this period of time and therefore analysis of the ionospheric boundary regions along the inbound and outbound orbit segments are carried out separately. The region where the flank boundary locations are observed is indicated by the light green line, and where the dayside boundary locations are found is indicated by the darker green line. Panel b shows the boundary region altitudes observed on the dayside ( $SZA < 80^\circ$ ), and panel c shows the boundary region altitudes observed at the flank ( $SZA \geq 80^\circ$ ) of the induced magnetosphere boundary. The light green and blue filled regions represent the error on the determined locations of the ICB and IMB, respectively. The location of the ICB (green) and IMB (blue) during the two DSW orbits where solar wind density was unusually low are indicated by stars.

Usually, the ICB is located near an altitude of 600 km on the day side of the planet. However, as the rarefaction region passed through the Martian induced magnetosphere, the subsolar and flank ICB extended to unusually high altitudes during the two DSW event orbits. This is shown in Figure 5 which depicts a 2D histogram of ICB locations spanning January 2015 through December 2018 in cylindrical MSO coordinates. The yellow dashed line indicates an altitude of 600 km, where more common occurrences of the ICB are seen at  $X > 0$  MSO locations. The location of the ICB flares outwards with increasing SZA from the subsolar point to  $90^\circ$  SZA. Near the flank region of the planet, the ICB is usually between 600 and 2,000 km, where an altitude of 2,000 km has been marked in Figure 5 by an orange dashed line.

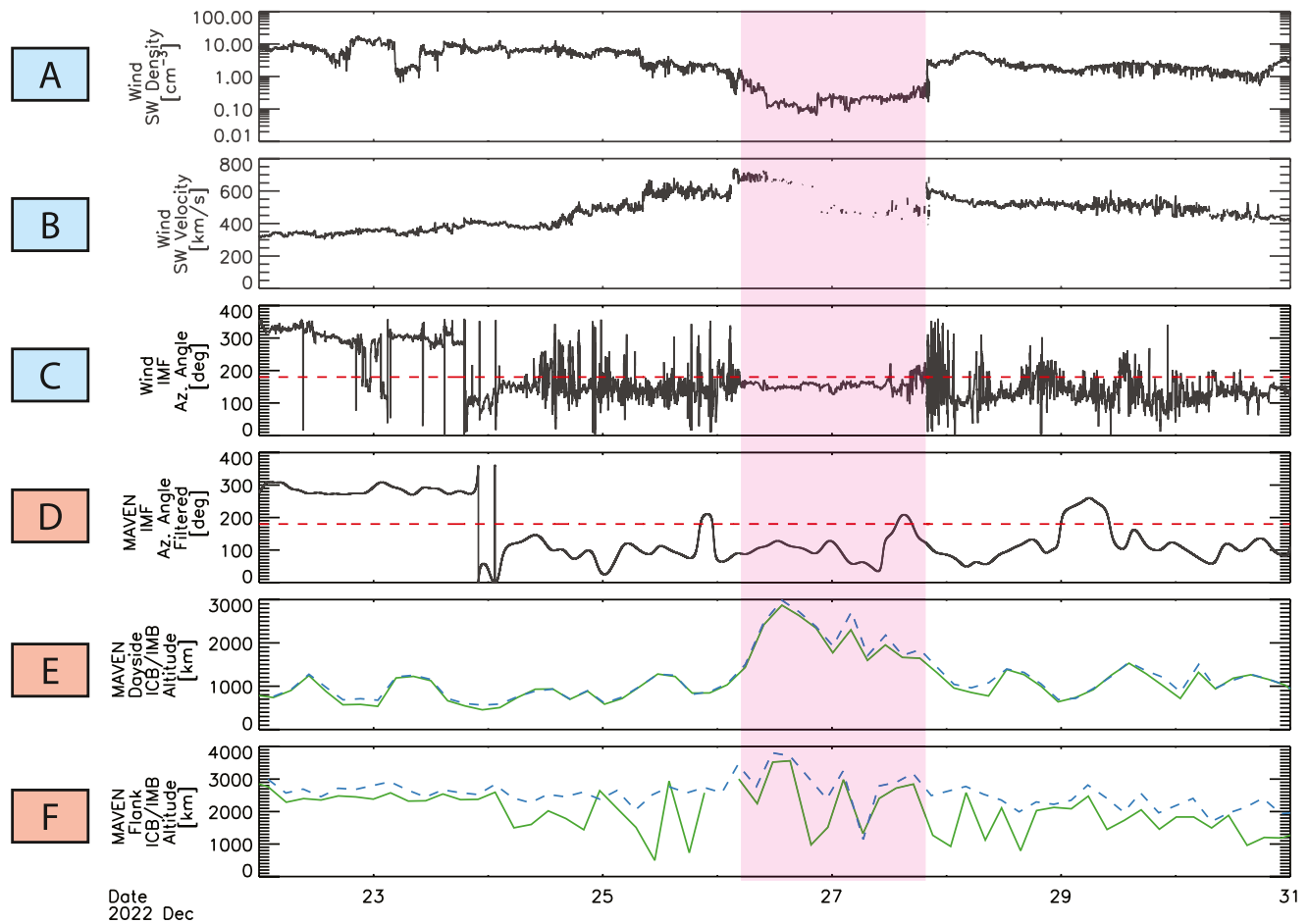


**Figure 5.** 2D histogram of ICB locations from January 2015 through December 2018. Each bin spans  $0.1 \times 0.1 R_{\text{Mars}}$  in MSO coordinates and has been normalized by the total number of observed ICB points. Lighter colors depict regions where the ICB is observed more often than bins of darker colors. The modeled bow shock and induced magnetosphere boundary determined in Vignes et al. (2000) are shown by the outer and inner black dashed lines, respectively. The yellow dashed line indicates an altitude of 600 km, and the orange dashed line indicates an altitude of 2,000 km. Mars is depicted as the black and white semi-circle, where the filled black side is used to show SZAs past the terminator. The cyan stars indicate the observed location of the ICB during the DSW event.

During the DSW event though, the ICB at  $10^\circ$  SZA is found outside the nominal bow shock derived from Vignes et al. (2000) at an altitude of  $\sim 2,900$  km. At the flank region, the ICB was observed at a maximum altitude of  $\sim 3,600$  km at  $92^\circ$  SZA during the DSW event. The maximum altitude instances of the ICB during the DSW event are indicated in Figure 5 by cyan stars, which show the unusually extended location of the ICB during this event. The expansion of the ICB during the DSW event is likely due to the very reduced solar wind dynamic pressure compressing the Martian induced magnetosphere, thereby permitting the expansion of the entire system (Halekas et al., 2023). However, after the rarefaction region has passed, the flank IMB and ICB continue to vary individually. This may indicate that the fluctuations in the ICB altitude during the period studied here are not solely due to changes in solar wind dynamic pressure.

Previous studies using Mars Express (MEX) data compared the effects of different solar wind conditions on the modeled conic shape of the ionosphere boundary (IB) (Ramstad et al., 2017). The IB is defined as the location where magnetosheath protons and alpha particles are not observed, and where a distinct and sustained appearance of cold, heavy ( $M/q \geq 16$ ) ion distributions exists. Because the ICB and IB are determined using similar criteria, the dynamics driving the IB location can be compared to the DSW event dynamics of the ICB that are observed with MAVEN data. Ramstad et al. (2017) found that the location of the IB was highly dependent on solar wind conditions. Interestingly, the nightside IB did not vary with dynamic pressure, but rather was found to expand with high solar wind velocity,  $u_{\text{SW}}$ , and compress with high solar wind density,  $n_{\text{SW}}$ . However, the fit algorithm from Ramstad et al. (2017) using the expected solar wind parameters from the DSW event ( $n_{\text{SW}} = 0.1 \text{ cm}^{-3}$  and  $u_{\text{SW}} \sim 400 \text{ km/s}$ ) did not match the observed locations of the flank ICB during the minimum solar wind proton orbits. Even after varying the solar wind parameters to account for systematic differences in the upstream solar wind estimates between MEX and MAVEN, the resulting fits did not match the DSW observations. This may indicate that other factors besides the solar wind velocity and density can drive the location of the flank ICB during events such as passing CIRs and rarefaction regions.

Within the CIR compression region and rarefaction region, solar wind density, velocity, and magnetic field magnitude all changed. However, when the large flank ICB altitude fluctuations began, the only large change in upstream driving conditions was in the azimuthal angle of the IMF. This is depicted in Figure 6. Panels a and b show the solar wind density and velocity derived using Wind data. Panel c depicts the azimuthal angle of the IMF from Wind MFI data, where azimuthal angle,  $\phi$ , is defined as the angle of the IMF in the X-Y ecliptic plane. An azimuthal angle of  $0^\circ$  indicates that the IMF is pointing radially toward the Sun, whereas an azimuthal angle of  $180^\circ$  indicates the IMF is pointing radially anti-sunward, neglecting the out-of-plane component of the IMF.



**Figure 6.** Time history showing the effect of solar wind and IMF conditions on the altitude of the Martian ICB and IMB. Panel a is the solar wind proton density from the Wind spacecraft. Panel b is the solar wind velocity magnitude from the Wind spacecraft. Panel c is the IMF azimuthal angle derived from Wind magnetic field data. All of the Wind data has been ballistically shifted to Mars' orbit. The horizontal red line represents an azimuthal angle of  $180^\circ$ . Panel d is the IMF azimuthal angle derived using MAVEN MAG data that has been bandpass filtered for periods between 4 hr and 6 days. The horizontal red line indicates an azimuthal angle of  $180^\circ$ . Panel e is the observed altitudes of the IMB (blue) and ICB (green) along the outbound segment (dayside location) of each MAVEN orbit. Panel f is the observed altitudes of the IMB and ICB along the inbound segment (flank location) of each MAVEN orbit. The pink tinted period represents the rarefaction region.

Panel d depicts the IMF azimuthal angle using MAVEN data. However, because MAVEN does not consistently sample the pristine solar wind, a bandpass filter allowing periods between 4 hr (longer than a MAVEN orbit) and 6 days was applied to full time history of the MAG azimuthal angle dataset. This separated the overarching IMF azimuthal angle from disturbances that occur within the induced magnetosphere or at periods less than a MAVEN orbit. Panels e and f depict the IMB and ICB altitude along the outbound (dayside) and inbound (flank) orbit segments, respectively, for this period of time for comparison to solar wind conditions.

Observations shown in Figure 6 indicate that the IMF azimuthal angle may drive the ICB dynamics observed over this period of time. From December 22–24th, when the flank IMB and ICB are observed to expand and contract together, the IMF azimuthal angle stays above  $180^\circ$ . This indicates that the IMF is in a toward sector orientation during this period, that is, sunward pointing with a -Y MSO (downward) magnetic field component. Then, when the IMF switches from having an azimuthal angle greater than  $180^\circ$  to an azimuthal angle less than  $180^\circ$  on 24 December 2022, the flank IMB and ICB (panel f) begin to decouple in altitude. Throughout the period where large fluctuations are observed in the ICB altitude, the IMF azimuthal angle remains in an away sector orientation, that is, anti-Sunward and duskward. The changes in solar wind proton density (panel a) and velocity (panel b) do not appear to influence whether the fluctuations in the flank ICB arise over this period of time, but may have implications for the magnitude of the fluctuations (Halekas et al., 2018).



## 6. Conclusion

In late December 2022, a CIR passed through the Martian induced magnetosphere. The compression region of the CIR at Mars caused an increase in solar wind dynamic pressure, heightened SEP populations, and higher values of thermal plasma pressure calculated using SWIA ion moments within the Martian ionosphere. The end of the CIR, which is marked by the point of highest solar wind velocity, passed through the Martian magnetosphere on December 26th.

Following the CIR was a rarefaction region of unusually low solar wind proton density. The low density values may be due to the solar wind originating from a coronal hole and active region on the Sun, which has led to other low solar wind density events in the past. This rarefaction region is responsible for the December 26th DSW event studied by Halekas et al. (2023).

Within the rarefaction region, the ICB and IMB expanded to high altitudes during the DSW event at Mars. In this period of unusually low solar wind proton densities, the IMB and ICB rise to a maximum altitude of 2,900 km near the subsolar point. The flank IMB expanded to a maximum altitude of 3,800 km, and the flank ICB expanded to a maximum altitude of 3,600 km during the minimum solar wind proton density orbits of the DSW event. Compared to a statistical study during solar minimum conditions, the ICB was observed to extend further than anything observed by the MAVEN spacecraft from January 2015 through December 2018.

The juxtaposition of the CIR compression region with the following rarefaction region allowed us to study the response of the Martian ionosphere to different solar wind conditions over a relatively short period of time. Because of the MAVEN orbit configuration, the boundary regions between shocked solar wind and ionospheric plasma were able to be sampled on the dayside and at the flank region of the induced magnetosphere between December 22 and 31.

The dayside ( $SZA < 80^\circ$ ) IMB and ICB changed altitudes in a similar way over the period of time between the CIR compression region and the trailing rarefaction region. The flank ICB and IMB, however, showed different variations in altitude from orbit to orbit ( $\sim 3.5$  hr). The flank ICB exhibited large fluctuations in altitude during this period of time compared to the flank IMB. A look at the upstream IMF and solar wind conditions revealed that a change in the azimuthal angle (in the XY MSO plane) of the IMF from  $\phi > 180^\circ$  to  $\phi < 180^\circ$  seemed to induce the large fluctuations seen in the ICB altitude.

This study highlights the dynamic nature of the Martian plasma environment in response to drastically changing solar wind and IMF conditions. Future studies on systematic correlations between the ICB and IMF conditions should be conducted, which would confirm if the difference in ICB altitudes is related to the changing IMF angle.

## Conflict of Interest

The authors declare no conflicts of interest relevant to this study.

## Data Availability Statement

The research described in this manuscript utilizes publicly available data from the MAVEN mission, including data from the SWIA, SWEA, MAG, STATIC, and SEP instruments. Data from the Wind SWE, MFI, and 3DP instruments was also used for context. All data were processed using the publicly available SPEDAS software (Angelopoulos et al., 2019). The MAVEN data used in this study are available through the Planetary Data System <https://pds-ppi.igpp.ucla.edu/mission/MAVEN>, Wind data is available through NASA's OMNIWeb site <https://omniweb.gsfc.nasa.gov/>, and the ADAPT-WSA ensemble set used for solar wind footprints can be found at <https://wsa-dashboard.helioanalytics.io/footprint>. Further information pertaining to the dataset and software used in this study can be found in the lead author's GitHub repository.

## References

- Acuña, M. H., Connerney, J. E. P., Wasilewski, P., Lin, R. P., Anderson, K. A., Carlson, C. W., et al. (1998). Magnetic field and plasma observations at mars: Initial results of the mars global surveyor mission. *Science*, 279(5357), 1676–1680. <https://doi.org/10.1126/science.279.5357.1676>
- Angelopoulos, V., Cruce, P., Drozdov, A., Grimes, E. W., Hatzigeorgiou, N., King, D. A., et al. (2019). The space physics environment data analysis system (SPEDAS). *Space Science Reviews*, 215(1), 9. <https://doi.org/10.1007/s11214-018-0576-4>

## Acknowledgments

The authors would like to thank the reviewers of this paper, Dr. Smitha Thampi and an anonymous reviewer, and the editor of the journal for their interest and helpful suggestions to improve this work. We thank the anonymous reviewer for directing us toward a charge state analysis using ACE data. We acknowledge NASA and the MAVEN mission for support partially through grant NNH10CC04C to the University of Colorado and by subcontract to Space Sciences Laboratory, University of California, Berkeley. Parts of this work for the observations obtained with the SWEA instrument are supported by the French space agency CNES (National Centre for Space Studies).



- Baker, D. N., Akasofu, S. I., Baumjohann, W., Bieber, J. W., Fairfield, E. W., Hones, W., Jr., et al. (1984). *Substorms in the magnetosphere, chapter 8. In Solar terrestrial physics-present and future* (Vol. 1120). NASA Pub.
- Bale, S. D., Drake, J. F., McManus, M. D., Desai, M. I., Badman, S. T., Larson, D. E., et al. (2023). Interchange reconnection as the source of the fast solar wind within coronal holes. *Nature*, 618(7964), 252–256. <https://doi.org/10.1038/s41586-023-05955-3>
- Bertucci, C., Mazelle, C., Acuña, M. H., Russell, C. T., & Slavin, J. A. (2005). Structure of the magnetic pileup boundary at mars and venus. *Journal of Geophysical Research Space Physics*, 110(A1). <https://doi.org/10.1029/2004ja010592>
- Bertucci, C., Mazelle, C., Crider, D. H., Vignes, D., Acuña, M. H., Mitchell, D. L., et al. (2003). Magnetic field draping enhancement at the martian magnetic pileup boundary from mars global surveyor observations. *Geophysical Research Letters*, 30(2). <https://doi.org/10.1029/2002gl015713>
- Boroyev, R. N., & Vasiliev, M. S. (2018). Substorm activity during the main phase of magnetic storms induced by the CIR and ICME events. *Advances in Space Research*, 61(1), 348–354. <https://doi.org/10.1016/j.asr.2017.10.031>
- Boscoboinik, G., Bertucci, C., Gomez, D., Morales, L., Mazelle, C., Halekas, J., et al. (2020). The magnetic structure of the subsolar MPB current layer from MAVEN observations: Implications for the hall electric force. *Geophysical Research Letters*, 47(21), e2020GL089230. <https://doi.org/10.1029/2020gl089230>
- Brain, D. A., Bagenal, F., Acuña, M. H., & Connerney, J. E. P. (2003). Martian magnetic morphology: Contributions from the solar wind and crust. *Journal of Geophysical Research*, 108(A12), 1424. <https://doi.org/10.1029/2002ja009482>
- Brain, D. A., Baker, A. H., Briggs, J., Eastwood, J. P., Halekas, J. S., & Phan, T.-D. (2010). Episodic detachment of martian crustal magnetic fields leading to bulk atmospheric plasma escape. *Geophysical Research Letters*, 37(14). <https://doi.org/10.1029/2010gl043916>
- Brain, D. A., Halekas, J. S., Peticolas, L. M., Lin, R. P., Luhmann, J. G., Mitchell, D. L., et al. (2006). On the origin of aurorae on mars. *Geophysical Series*, 33(1), L01201. <https://doi.org/10.1029/2005gl024782>
- Brain, D. A., Mitchell, D. L., & Halekas, J. S. (2006). The magnetic field draping direction at mars from April 1999 through August 2004. *Icarus*, 182(2), 464–473. <https://doi.org/10.1016/j.icarus.2005.09.023>
- Breus, T. K., Krymskii, A. M., Lundin, R., Dubinin, E. M., Luhmann, J. G., Yeroshenko, Y. G., et al. (1991). The solar wind interaction with mars: Consideration of phobos 2 mission observations of an ion composition boundary on the dayside. *Journal of Geophysical Research*, 96(A7), 11165–11174. <https://doi.org/10.1029/91ja01131>
- Bürgi, A., & Geiss, J. (1986). Helium and minor ions in the corona and solar wind: Dynamics and charge states. *Solar Physics*, 103(2), 347–383. <https://doi.org/10.1007/bf00147835>
- Cane, H. V., & Richardson, I. G. (2003). Interplanetary coronal mass ejections in the near-earth solar wind during 1996–2002. *Journal of Geophysical Research*, 108(A4), 1156. <https://doi.org/10.1029/2002ja009817>
- Connerney, J. E. P., Acuña, M. H., Wasilewski, P. J., Kletetschka, G., Ness, N. F., Rème, H., et al. (2001). The global magnetic field of mars and implications for crustal evolution. *Geophysical Research Letters*, 28(No. 21), 4015–4018. <https://doi.org/10.1029/2001gl013619>
- Connerney, J. E. P., Espley, J., Lawton, P., Murphy, S., Odom, J., Oliverson, R., & Sheppard, D. (2015). The MAVEN magnetic field investigation. *Space Science Reviews*, 195(1), 257–291. <https://doi.org/10.1007/s11214-015-0169-4>
- Cranmer, S. R. (2009). Coronal holes. *Living Reviews in Solar Physics*, 6, 3. <https://doi.org/10.12942/lrsp-2009-3>
- Cravens, T. E. (1997). *Physics of solar system plasmas*. Cambridge University Press.
- Da Silva, D. E., Wallace, S., Arge, C. N., & Jones, S. (2023). Ensemble forecasts of solar wind connectivity to 1  $r_s$  using ADAPT-WSA. *Space Weather*, 21(10). <https://doi.org/10.1029/2023sw003554>
- Dubinin, E., Fraenz, M., Woch, J., Duru, F., Gurnett, D., Modolo, R., et al. (2009). Ionospheric storms on mars: Impact of the corotating interaction region. *Geophysical Research Letters*, 36(1), L01105. <https://doi.org/10.1029/2008gl036559>
- Dubinin, E., Fränz, M., Woch, J., Roussos, E., Barabash, S., Lundin, R., et al. (2006). Plasma morphology at mars. aspera-3 observations. *Space Science Reviews*, 126(1), 209–238. <https://doi.org/10.1007/s11214-006-9039-4>
- Dubinin, E., Lundin, R., Fränz, M., Woch, J., Barabash, S., Fedorov, A., et al. (2006). Electric fields within the martian magnetosphere and ion extraction: ASPERA-3 observations. *Icarus*, 182(2), 337–342. <https://doi.org/10.1016/j.icarus.2005.05.022>
- Eastwood, J. P., Hietala, H., Toth, G., Phan, T. D., & Fujimoto, M. (2015). What controls the structure and dynamics of earth's magnetosphere? *Space Science Reviews*, 188(1–4), 251–286. <https://doi.org/10.1007/s11214-014-0050-x>
- Edberg, N., Nilsson, H., Williams, A. O., Lester, M., Milan, S. E., Cowley, S. W. H., et al. (2010). Pumping out the atmosphere of mars through solar wind pressure pulses. *Geophysical Research Letters*, 37(3), L03107. <https://doi.org/10.1029/2009gl041814>
- Gonzalez, W. D., & Tsurutani, B. T. (1987). Criteria of interplanetary parameters causing intense magnetic storms (dst < -100 nt). *Planetary and Space Science*, 35(9), 1101–1109. [https://doi.org/10.1016/0032-0633\(87\)90015-8](https://doi.org/10.1016/0032-0633(87)90015-8)
- Gosling, J. T., Hundhausen, A. J., Pizzo, V., & Asbridge, J. R. (1972). Compressions and rarefactions in the solar wind: Vela 3. *Journal of Geophysical Research*, 77(28), 5442–5454. <https://doi.org/10.1029/ja077i028p05442>
- Gunell, H., Amerstorfer, U. V., Nilsson, H., Grima, C., Koepke, M., Fränz, M., et al. (2008). Shear driven waves in the induced magnetosphere of mars. *Plasma Physics and Controlled Fusion*, 50(7), 074018. <https://doi.org/10.1088/0741-3335/50/7/074018>
- Gurnett, D. A., Morgan, D. D., Duru, F., Akalin, F., Winningham, J. D., Frahm, R. A., et al. (2010). Large density fluctuations in the martian ionosphere as observed by the mars express radar sounder. *Icarus*, 206(1), 83–94. <https://doi.org/10.1016/j.icarus.2009.02.019>
- Halekas, J. S., Brain, D. A., Ruhunusiri, S., McFadden, J. P., Mitchell, D. L., Mazelle, C., et al. (2016). Plasma clouds and snowplows: Bulk plasma escape from mars observed by MAVEN. *Geophysical Research Letters*, 43(4), 1426–1434. <https://doi.org/10.1002/2016gl067752>
- Halekas, J. S., McFadden, J. P., Brain, D. A., Luhmann, J. G., DiBraccio, G. A., Connerney, J. E. P., et al. (2018). Structure and variability of the martian ion composition boundary layer. *Journal of Geophysical Research Space Physics*, 123(10), 8439–8458. <https://doi.org/10.1029/2018ja025866>
- Halekas, J. S., Ruhunusiri, S., Harada, Y., Collinson, G., Mitchell, D. L., Mazelle, C., et al. (2017). Structure, dynamics, and seasonal variability of the mars-solar wind interaction: MAVEN solar wind ion analyzer in-flight performance and science results. *Journal of Geophysical Research Space Physics*, 122(1), 547–578. <https://doi.org/10.1002/2016ja023167>
- Halekas, J. S., Ruhunusiri, S., McFadden, J. P., Espley, J. R., & DiBraccio, G. A. (2019). Ion composition boundary layer instabilities at mars. *Geophysical Research Letters*, 46(17–18), 10303–10312. <https://doi.org/10.1029/2019gl084779>
- Halekas, J. S., Shaver, S., Azari, A. R., Fowler, C. M., Ma, Y., Xu, S., et al. (2023). The day the solar wind disappeared at mars. *Journal of Geophysical Research Space Physics*, 128(12), e2023JA031935. <https://doi.org/10.1029/2023ja031935>
- Halekas, J. S., Taylor, E. R., Dalton, G., Johnson, G., Curtis, D. W., McFadden, J. P., et al. (2015). The solar wind ion analyzer for MAVEN. *Space Science Reviews*, 195(1), 125–151. <https://doi.org/10.1007/s11214-013-0029-z>
- Hamil, O., Cravens, T. E., Renzaglia, A., & Andersson, L. (2022). Small scale magnetic structure in the induced martian ionosphere and lower magnetic pile-up region. *Journal of Geophysical Research Space Physics*, 127(4), e2021JA030139. <https://doi.org/10.1029/2021ja030139>

- Heidrich-Meisner, V., Peleikis, T., Kruse, M., Berger, L., & Wimmer-Schweingruber, R. (2016). Observations of high and low Fe charge states in individual solar wind streams with coronal-hole origin. *Astronomy & Astrophysics, Supplement Series*, 593, A70. <https://doi.org/10.1051/0004-6361/201527998>
- Holmberg, M. K. G., André, N., Garnier, P., Modolo, R., Andersson, L., Halekas, J., et al. (2019). MAVEN and MEX multi-instrument study of the dayside of the martian induced magnetospheric structure revealed by pressure analyses. *Journal of Geophysical Research Space Physics*, 124(11), 8564–8589. <https://doi.org/10.1029/2019ja026954>
- Huang, H., Guo, J., Wang, Z., Lin, H., Zheng, J., Cui, J., et al. (2019). Properties of stream interactions and their associated shocks near 1.52 au: MAVEN observations. *ApJ*, 879(2), 118. <https://doi.org/10.3847/1538-4357/ab25e9>
- Hudson, H. S., Mulay, S. M., Fletcher, L., Docherty, J., Fitzpatrick, J., Pike, E., et al. (2022). Fast prograde coronal flows in solar active regions. *Mon. Not. R. Astron. Soc. Lett.*, 515(1), L84–L88. <https://doi.org/10.1093/mnrasl/slac079>
- Hundhausen, A. J. (1972). *Coronal expansion and solar wind*. Springer Berlin Heidelberg.
- Jakosky, B., Lin, R. P., Grebowsky, J. M., Luhmann, J. G., Mitchell, D. F., Beutelschies, G., et al. (2015). The Mars atmosphere and volatile evolution (MAVEN) mission. *Space Science Reviews*, 195(1), 3–48. <https://doi.org/10.1007/s11214-015-0139-x>
- Janardhan, P., Fujiki, K., Sawant, H. S., Kojima, M., Hakamada, K., & Krishnan, R. (2008). Source regions of solar wind disappearance events. *Journal of Geophysical Research: Space Physics*, 113(A3), A03102. <https://doi.org/10.1029/2007ja012608>
- Janardhan, P., Tripathi, D., & Mason, H. E. (2008). The solar wind disappearance event of 11 May 1999: Source region evolution. *Astronomy & Astrophysics, Supplement Series*, 488(1), L1–L4. <https://doi.org/10.1051/0004-6361:200809667>
- Jian, L. K., Luhmann, J. G., Russell, C. T., & Galvin, A. B. (2019). Solar terrestrial relations observatory (STEREO) observations of stream interaction regions in 2007–2016: Relationship with heliospheric current sheets, solar cycle variations, and dual observations. *Solar Physics*, 294(3), 31. <https://doi.org/10.1007/s11207-019-1416-8>
- Jian, L. K., Russell, C. T., Luhmann, J. G., MacNeice, P. J., Odstrcil, D., Riley, P., et al. (2011). Comparison of observations at ACE and Ulysses with ENLIL model results: Stream interaction regions during Carrington rotations 2016–2018. *Solar Physics*, 273(1), 179–203. <https://doi.org/10.1007/s11207-011-9858-7>
- Jian, L. K., Russell, C. T., Luhmann, J. G., & Skoug, R. M. (2006). Properties of stream interactions at one AU during 1995–2004. *Solar Physics*, 239(1), 337–392. <https://doi.org/10.1007/s11207-006-0132-3>
- Kivelson, M. G., & Russell, C. T. (1995). *Introduction to space physics*. Cambridge University Press.
- Kojima, M., Fujiki, K., Ohmi, T., Tokumaru, M., Yokobe, A., & Hakamada, K. (1999). Low-speed solar wind from the vicinity of solar active regions. *Journal of Geophysical Research*, 104(A8), 16993–17003. <https://doi.org/10.1029/1999ja000177>
- Krishnaprasad, C., Thampi, S. V., Bhardwaj, A., Pant, T. K., & Thampi, R. S. (2021). Ionospheric plasma energization at Mars during the September 2017 ICME event. *Planetary and Space Science*, 205, 105291. <https://doi.org/10.1016/j.pss.2021.105291>
- Larson, D. E., Lillis, R. J., Lee, C. O., Dunn, P. A., Hatch, K., Robinson, M., et al. (2015). The MAVEN solar energetic particle investigation. *Space Science Reviews*, 195(1–4), 153–172. <https://doi.org/10.1007/s11214-015-0218-z>
- Lee, C. O., Hara, T., Halekas, J. S., Thiemann, E., Chamberlin, P., Eparvier, F., et al. (2017). MAVEN observations of the solar cycle 24 space weather conditions at Mars. *Journal of Geophysical Research Space Physics*, 122(3), 2768–2794. <https://doi.org/10.1002/2016ja023495>
- Lee, C. O., Jakosky, B. M., Luhmann, J. G., Brain, D. A., Mays, M. L., Hassler, D. M., et al. (2018). Observations and impacts of the 10 September 2017 solar events at Mars: An overview and synthesis of the initial results. *Geophysical Research Letters*, 45(17), 8871–8885. <https://doi.org/10.1029/2018gl079162>
- Lentz, C. L., Baker, D. N., Andersson, L., Thaller, S., Fowler, C. M., & Leonard, T. W. (2021). The effects of different drivers on the induced Martian magnetosphere boundary: A case study of September 2017. *Journal of Geophysical Research Space Physics*, 126(2), e2020JA028105. <https://doi.org/10.1029/2020ja028105>
- Lepping, R. P., Acuña, M. H., Burlaga, L. F., Farrell, W. M., Slavin, J. A., Schatten, K. H., et al. (1995). The WIND magnetic field investigation. *Space Science Reviews*, 71(1–4), 207–229. <https://doi.org/10.1007/bf00751330>
- Lepri, S. T., Zurbuchen, T. H., Fisk, L. A., Richardson, I. G., Cane, H. V., & Gloeckler, G. (2001). Iron charge distribution as an identifier of interplanetary coronal mass ejections. *Journal of Geophysical Research*, 106(A12), 29231–29238. <https://doi.org/10.1029/2001ja000014>
- Lin, R. P., Anderson, K. A., Ashford, S., Carlson, C., Curtis, D., Ergun, R., et al. (1995). A three-dimensional plasma and energetic particle investigation for the wind spacecraft. *Space Science Reviews*, 71(1–4), 125–153. <https://doi.org/10.1007/bf00751328>
- Luhmann, J. G. (1992). Comparative studies of the solar wind interaction with weakly magnetized planets. *Advances in Space Research*, 12(9), 191–203. [https://doi.org/10.1016/0273-1177\(92\)90331-q](https://doi.org/10.1016/0273-1177(92)90331-q)
- Luhmann, J. G., & Brace, L. H. (1991). Near? Mars space. *Review of Geophysics*, 29(2), 121–140. <https://doi.org/10.1029/91rg00066>
- Luhmann, J. G., Li, Y., Arge, C. N., Gazis, P. R., & Ulrich, R. (2002). Solar cycle changes in coronal holes and space weather cycles. *Journal of Geophysical Research*, 107(A8), 1154. <https://doi.org/10.1029/2001ja007550>
- Lundin, R., Barabash, S., Andersson, H., Holmström, M., Grigoriev, A., Yamauchi, M., et al. (2004). Solar wind-induced atmospheric erosion at Mars: First results from ASPERA-3 on Mars Express. *Science*, 305(5692), 1933–1936. <https://doi.org/10.1126/science.1101860>
- Lundin, R., Barabash, S., Dubinin, E., Winningham, D., & Yamauchi, M. (2011). Low-altitude acceleration of ionospheric ions at Mars. *Geophysical Research Letters*, 38(8), L08108. <https://doi.org/10.1029/2011gl047064>
- Ma, Y. J., Fang, X., Nagy, A. F., Russell, C. T., & Toth, G. (2014). Martian ionospheric responses to dynamic pressure enhancements in the solar wind. *Journal of Geophysical Research Space Physics*, 119(2), 1272–1286. <https://doi.org/10.1002/2013ja019402>
- Matsunaga, K., Seki, K., Brain, D. A., Hara, T., Masunaga, K., McFadden, J. P., et al. (2017). Statistical study of relations between the induced magnetosphere, ion composition, and pressure balance boundaries around Mars based on MAVEN observations. *Journal of Geophysical Research Space Physics*, 122(9), 9723–9737. <https://doi.org/10.1002/2017ja024217>
- McFadden, J. P., Kortmann, O., Curtis, D., Dalton, G., Johnson, G., Abiad, R., et al. (2015). MAVEN SupraThermal and thermal ion composition (STATIC) instrument. *Space Science Reviews*, 195(1), 199–256. <https://doi.org/10.1007/s11214-015-0175-6>
- Mitchell, D. L., Lin, R. P., Mazelle, C., Rème, H., Cloutier, P. A., Connerney, J. E. P., et al. (2001). Probing Mars' crustal magnetic field and ionosphere with the MGS electron reflectometer. *Journal of Geophysical Research*, 106(E10), 23419–23427. <https://doi.org/10.1029/2000je001435>
- Mitchell, D. L., Mazelle, C., Sauvaud, J.-A., Thocaven, J.-J., Rouzaud, J., Fedorov, A., et al. (2016). The MAVEN solar wind electron analyzer. *Space Science Reviews*, 200(1), 495–528. <https://doi.org/10.1007/s11214-015-0232-1>
- Morschhauser, A., Vervelidou, F., Thomas, P., Grott, M., Lesur, V., & Gilder, S. A. (2018). Mars' crustal magnetic field.
- Neugebauer, M., Liewer, P. C., Goldstein, B. E., Zhou, X., & Steinberg, J. T. (2004). Solar wind stream interaction regions without sector boundaries. *JGR: Space Physics*, 109(A10), A10102. <https://doi.org/10.1029/2004ja010456>
- Ogilvie, K. W., Chornay, D. J., Fritzenreiter, R. J., Hunsaker, F., Keller, J., Lobell, J., et al. (1995). SWE, a comprehensive plasma instrument for the WIND spacecraft. *Space Science Reviews*, 71(1–4), 55–77. <https://doi.org/10.1007/bf00751326>

- Owens, M. J. (2020). Solar-Wind structure. In *Oxford research encyclopedia of physics*. <https://doi.org/10.1093/acrefore/9780190871994.013.19>
- Parker, E. N. (1965). Dynamical theory of the solar wind. *Space Science Reviews*, 4(5), 666–708. <https://doi.org/10.1007/bf00216273>
- Ramstad, R., Barabash, S., Futaana, Y., & Holmström, M. (2017). Solar wind?and EUV?dependent models for the shapes of the martian plasma boundaries based on mars express measurements. *Journal of Geophysical Research: Space Physics*, 122(7), 7279–7290. <https://doi.org/10.1002/2017ja024098>
- Ramstad, R., Brain, D. A., Dong, Y., Espley, J., Halekas, J., & Jakosky, B. (2020). The global current systems of the martian induced magnetosphere. *Nature Astronomy*, 4(10), 979–985. <https://doi.org/10.1038/s41550-020-1099-y>
- Richardson, I. G. (2004). Energetic particles and corotating interaction regions in the solar wind. *Space Science Reviews*, 111(3), 267–376. <https://doi.org/10.1023/b:spac.0000032689.52830.3e>
- Richardson, I. G. (2018). Solar wind stream interaction regions throughout the heliosphere. *Living Reviews in Solar Physics*, 15(1), 1. <https://doi.org/10.1007/s41116-017-0011-z>
- Richardson, I. G., & Cane, H. V. (2004). Identification of interplanetary coronal mass ejections at 1 AU using multiple solar wind plasma composition anomalies. *Journal of Geophysical Research*, 109(A9), A09104. <https://doi.org/10.1029/2004ja010598>
- Richardson, I. G., & Cane, H. V. (2010). Near-earth interplanetary coronal mass ejections during solar cycle 23 (1996 – 2009): Catalog and summary of properties. *Solar Physics*, 264(1), 189–237. <https://doi.org/10.1007/s11207-010-9568-6>
- Sarabhai, V. (1963). Some consequences of nonuniformity of solar wind velocity. *Journal of Geophysical Research*, 68(5), 1555–1557. <https://doi.org/10.1029/jz068i005p01555>
- Schrijver, C. J., & DeRosa, M. L. (2003). Photospheric and heliospheric magnetic fields. *Solar Physics*, 212(1), 165–200. <https://doi.org/10.1023/a:1022908504100>
- Smith, E. J., & Wolfe, J. H. (1976). Observations of interaction regions and corotating shocks between one and five AU: Pioneers 10 and 11. *Geophysical Research Letters*, 3, 137–140. <https://doi.org/10.1029/gl003i003p00137>
- Snyder, C. W., Neugebauer, M., & Rao, U. R. (1963). The solar wind velocity and its correlation with cosmic-ray variations and with solar and geomagnetic activity. *Journal of Geophysical Research*, 68(24), 6361–6370. <https://doi.org/10.1029/jz068i024p06361>
- Stansby, D., Green, L. M., Van Driel-Gesztelyi, L., & Horbury, T. S. (2021). Active region contributions to the solar wind over multiple solar cycles. *Solar Physics*, 296(8), 116. <https://doi.org/10.1007/s11207-021-01861-x>
- Stone, E. C., Frandsen, A. M., Mewaldt, R. A., Christian, E. R., Margolies, D., Ormes, J. F., & Snow, F. (1998). The advanced composition explorer. *Space Science Reviews*, 1–22. [https://doi.org/10.1007/978-94-011-4762-0\\_1](https://doi.org/10.1007/978-94-011-4762-0_1)
- SWICS 2.0 level 2 data documentation. (2007). Retrieved from [https://izw1.caltech.edu/ACE/ASC/level2/ss2\\_12desc.html](https://izw1.caltech.edu/ACE/ASC/level2/ss2_12desc.html)
- Szegö, K., Glassmeier, K.-H., Bingham, R., Bogdanov, A., Fischer, C., Haerendel, G., & Zank, G. (2000). Physics of mass loaded plasmas. *Space Science Reviews*, 94(3), 429–671. <https://doi.org/10.1023/a:1026568530975>
- Thampi, S. V., Krishnaprasad, C., Shreedevi, P. R., Pant, T. K., & Bhardwaj, A. (2019). Acceleration of energetic ions in corotating interaction region near 1.5 au: Evidence from MAVEN. *ApJL*, 880(1), L3. <https://doi.org/10.3847/2041-8213/ab2b43>
- Tsurutani, B. T., Gonzalez, W. D., Gonzalez, W. D., Lu, G., Sobral, J. H. A., & Gopalswamy, N. (2006). Corotating solar wind streams and recurrent geomagnetic activity: A review. *Journal of Geophysical Research*, 111(A07S01). <https://doi.org/10.1029/2006ja011745>
- Van Driel-Gesztelyi, L., & Green, L. M. (2015). Evolution of active regions. *Living Reviews in Solar Physics*, 12(1), 1. <https://doi.org/10.1007/lrsp-2015-1>
- Vignes, D., Mazelle, C., Rme, H., Acuña, M. H., Connerney, J. E. P., Lin, R. P., et al. (2000). The solar wind interaction with mars: Locations and shapes of the bow shock and the magnetic pile-up boundary from the observations of the MAG/ER experiment onboard mars global surveyor. *Geophysical Research Letters*, 27(No. 1), 49–52. <https://doi.org/10.1029/1999gl010703>
- Xu, S., Liemohn, M. W., Dong, C., Mitchell, D. L., Bougher, S. W., & Ma, Y. (2016). Pressure and ion composition boundaries at mars. *Journal of Geophysical Research Space Physics*, 121(7), 6417–6429. <https://doi.org/10.1002/2016ja022644>
- Xu, S., Mitchell, D. L., McFadden, J. P., Fowler, C. M., Hanley, K., Weber, T., et al. (2023). Photoelectron boundary: The top of the dayside ionosphere at mars. *Journal of Geophysical Research Space Physics*, 128(5). <https://doi.org/10.1029/2023ja031353>
- Zirker, J. B. (1977). Coronal holes and high-speed wind streams. *Review of Geophysics*, 15(3), 257–269. <https://doi.org/10.1029/rg015i003p00257>
- Zurbuchen, T. H., Fisk, L. A., Gloeckler, G., & Von Steiger, R. (2002). The solar wind composition throughout the solar cycle: A continuum of dynamic states. *Geophysical Research Letters*, 29(9), 1352. <https://doi.org/10.1029/2001gl013946>